



Noninvasive estimation of aortic pressure waveform based on simplified Kalman filter and dual peripheral artery pressure waveforms

Wenyan Liu^a, Shuo Du^a, Shuran Zhou^a, Tiemin Mei^{d,*}, Yuelan Zhang^e, Guozhe Sun^e, Shuang Song^f, Lisheng Xu^{a,b,c,*}, Yudong Yao^a, Stephen E. Greenwald^g

^a College of Medicine and Biological and Information Engineering, Northeastern University, Shenyang 110169, China

^b Key Laboratory of Medical Image Computing, Ministry of Education, Shenyang 110169, China

^c Neusoft Research of Intelligent Healthcare Technology, Co. Ltd., Shenyang 110169, China

^d School of Automation and Electrical Engineering, Shenyang Ligong University, Shenyang 110159, China

^e First Hospital of China Medical University, Shenyang 110122, China

^f School of Mechanical Engineering and Automation, Harbin Institute of Technology Shenzhen Graduate School, Shenzhen 518055, China

^g Blizard Institute, Barts & The London School of Medicine & Dentistry, Queen Mary University of London, United Kingdom

ARTICLE INFO

Article history:

Received 17 October 2021

Revised 6 March 2022

Accepted 14 March 2022

Keywords:

Aortic pressure

Peripheral artery pressure

Simplified Kalman filter

Canonical correlation analysis

Signal-to-noise ratio

Noise-tolerance

ABSTRACT

Background and Objective: Aortic pressure (P_a) is important for the diagnosis of cardiovascular disease. However, its direct measurement is invasive, not risk-free, and relatively costly. In this paper, a new simplified Kalman filter (SKF) algorithm is employed for the reconstruction of the P_a waveform using dual peripheral artery pressure waveforms.

Methods: P_a waveforms obtained in a previous study were collected from 25 patients. Simultaneously, radial and femoral pressure waveforms were generated from two simulation experiments, using transfer functions. In the first, the transfer function is a known finite impulse response; and in the second, it is derived from a tube-load model. To analyze the performance of the proposed SKF algorithm, variable amounts of noise were added to the observed output signal, to give a range of signal-to-noise ratios (SNRs). Additionally, central aortic, brachial and femoral pressure waveforms were simultaneously collected from 2 Sprague-Dawley rats and the measured and reconstructed P_a waveforms were compared.

Results: The proposed SKF algorithm outperforms canonical correlation analysis (CCA), which is the current state-of-the-art blind system identification method for the non-invasive estimation of central aortic blood pressure. It is also shown that the proposed SKF algorithm is more noise-tolerant than the CCA algorithm over a wide range of SNRs.

Conclusion: The simulations and animal experiments illustrate that the proposed SKF algorithm is accurate and stable in the face of low SNRs. Improved methods for estimating central blood pressure as a measure of cardiac load adds to their value as a prognostic and diagnostic tool.

© 2022 Elsevier B.V. All rights reserved.

1. Introduction

The aortic pressure (P_a) waveform is an important predictor of cardiovascular disease risk [1]. The blood ejected from the left ventricle gives rise to an aortic pressure wave which is propagated through the arterial tree changing in amplitude and shape as it progresses, in a way which depends on variations in the local diameter, wall thickness and elastic properties of the aorta, as well as the presence of reflected waves from peripheral sites and, to a

lesser extent, on re-reflections [2,3]. Thus P_a , having been formed initially at the aortic root by the contraction of the left ventricle, contains essential information about the heart itself as well as about the properties of the arterial system in general [4,5]. P_a in the ascending aorta, often referred to as “central pressure” is of particular importance because it is a measure of maximal left ventricular load [6]. However, the use of P_a as a diagnostic and prognostic tool has been limited in clinical practice because the gold standard of P_a measurement using a pressure-sensing cardiac catheter is invasive and expensive [7]. Therefore, a number of non-invasive measurement techniques have been proposed, usually substitution and transfer function methods, in which the central pressure wave is derived from peripheral pressure measurements.

* Corresponding author.

E-mail addresses: meitiemin@163.com (T. Mei), xuls@bmie.neu.edu.cn (L. Xu).

Abbreviations

CCA	Canonical correlation analysis
CR	Cross-relation
C_T	Compliance of the distal arteries
DP	Diastolic pressure
FIR	Finite impulse response
MBSI	Multichannel blind system identification
NPM	Normalized projection misalignment
P_a	Aortic pressure
P_b	Brachial pressure
P_f	Femoral pressure
P_p	Peripheral artery pressure
P_r	Radial pressure
R_T	Peripheral resistance
RMSE	Root mean square error
SIMO	Single input multiple output
SKF	Simplified Kalman filter
SP	Systolic pressure
SS	Subspace
TW	Total waveform
Z_c	Characteristic impedance
Z_L	Terminal impedance

Peripheral artery pressure (P_p) waveforms such as the brachial pressure (P_b) are generally easier to obtain noninvasively than the P_a waveform. However, due to the aforementioned changes in shape as the wave propagates along the arterial tree, important aspects of the P_a waveform, such as systolic pressure and pulse pressure cannot be accurately derived from the measurement of peripheral artery pressure [8]. Carotid pressure is also often used as a surrogate for central P_a because the carotid artery is closer to the aorta than the brachial artery. However, even the carotid pressure waveform is subject to amplification and, in general, will lead to an over-estimation of central P_a [9,10]. Several numerical methods to estimate the P_a from non-invasive measurements of P_p have recently been developed. A widely used approach is based on the notion of a generalized transfer function. This is obtained from simultaneous measurements of P_a (invasive) and P_p (non-invasive) on a large number of subjects [11,12,15,16]. The inverse transfer function can then be derived and used to estimate P_a from P_p . Tube-load models represent the path between the aorta and the periphery from which a transfer function can be derived for the P_a waveform [13,14]. However, generalized transfer function methods require parameter values derived from prior invasively measured central pressures from many subjects [15]. Additionally, the form of the function will depend on the specific measurement device and thus care should be taken to allow for this [15]. Furthermore, it is usually assumed that the arterial system is linear and short-time invariant. In spite of these limitations, such methods have proved to be useful as a means of estimating systolic pressure although pulse pressure estimation is less reliable [17]. More recently, multichannel blind system identification (MBSI) algorithms have been proposed, such as the cross-relation (CR) algorithm [18], the subspace (SS) algorithm [19], and the canonical correlation analysis (CCA) algorithm [20]. These methods are able to estimate the P_a waveform satisfactorily when the signal-to-noise ratio (SNR) of the observed channel output is high [21]. Unfortunately, the peripheral artery pressure signal may contain some noise and the SNR may not be high enough. In this paper, we propose a simplified Kalman filter (SKF) algorithm for P_a waveform estimation with a high update rate and which is tolerant of low SNRs. The main innovations of the study are as follows: 1) the central aortic pressure waveform is noninvasively estimated by two peripheral pressure waveforms,

Table 1

Basic information of the clinical data (Mean \pm SD).

Variables	Data
Gender, male/female	10/15
Age (years)	56.8 \pm 13.5
Height (cm)	165.4 \pm 7.9
Weight (kg)	68.6 \pm 12.4
SP (mmHg)	147.3 \pm 20.7
DP (mmHg)	76.8 \pm 11.5
HR (bpm)	74.0 \pm 4.8

and 2) the proposed method is self-calibrating and accommodates any inter-subject variation and intra-subject differences in vascular dynamics.

The paper is organized as follows. Section 2 describes the data acquisition, the estimation of the P_a by the MBSI method, evaluation indices and statistical analysis. Section 3 presents the results, which are discussed and interpreted in Section 4. Section 5 concludes the paper with suggestions for future work.

2. Methods

In this paper, the CCA algorithm [20] based on a linear single input multiple output (SIMO) system is applied as a benchmark to compare the performance of different blind system identification algorithms. The generated peripheral artery pressure waveforms as the observed output signals using the finite impulse response (FIR) and tube-load simulation models are noiseless. It has been reported that the majority of real pulse waveforms have SNRs between 50 dB and 10 dB with only 8% above 50 dB and only 1.5% below 10 dB [22]. Therefore, to analyze and compare the performance of the SKF and CCA algorithms, various levels of noise (Gaussian random) in the range 10 dB to 50 dB were added to the observed output signals. Respiration was simulated by modulating the baseline with a sinusoidal signal [22] and these noisy signals were used in the simulation experiments. With this in mind, the resulting pulse signal can be modeled as:

$$x_i(n) = p_{pi}(n) + b_{1i}(n) + b_{2i}(n) \quad (1)$$

As shown in Fig. 1, $p_{pi}(n)$ represents the heart-generated pulse wave signal. $b_{1i}(n)$ and $b_{2i}(n)$ represent the respiratory modulation signal and Gaussian random noise signal, respectively.

$$b_{1i}(n) = a_1 \sin(2\pi f_0 n / F_s) \quad (2)$$

where a_1 and f_0 are the amplitude and frequency of the simulated respiratory sinusoidal signal. Clinical observations have shown that the healthy human pulse rate is four to five times the respiration rate [23]. Therefore, f_0 was set to 0.3 Hz and the value of a_1 was chosen according to the magnitude of the SNR.

2.1. Data acquisition

Here, we have utilized a set of clinical data collected in a previous study [24,40]. Invasive measurements of central P_a were made at the aortic root in 25 patients undergoing cardiac surgery, at a sampling frequency of 100 Hz. Basic population and hemodynamic data are listed in Table 1. Approval was obtained from the Research Ethics Committee of the Northeastern University (EC-2020B016), China, and written informed consent was obtained from all participants.

2.1.1. Simulation data generated with the FIR model

As shown in Fig. 2, the simulated radial pressure (P_r) and femoral pressure (P_f) waveforms without noise were obtained as

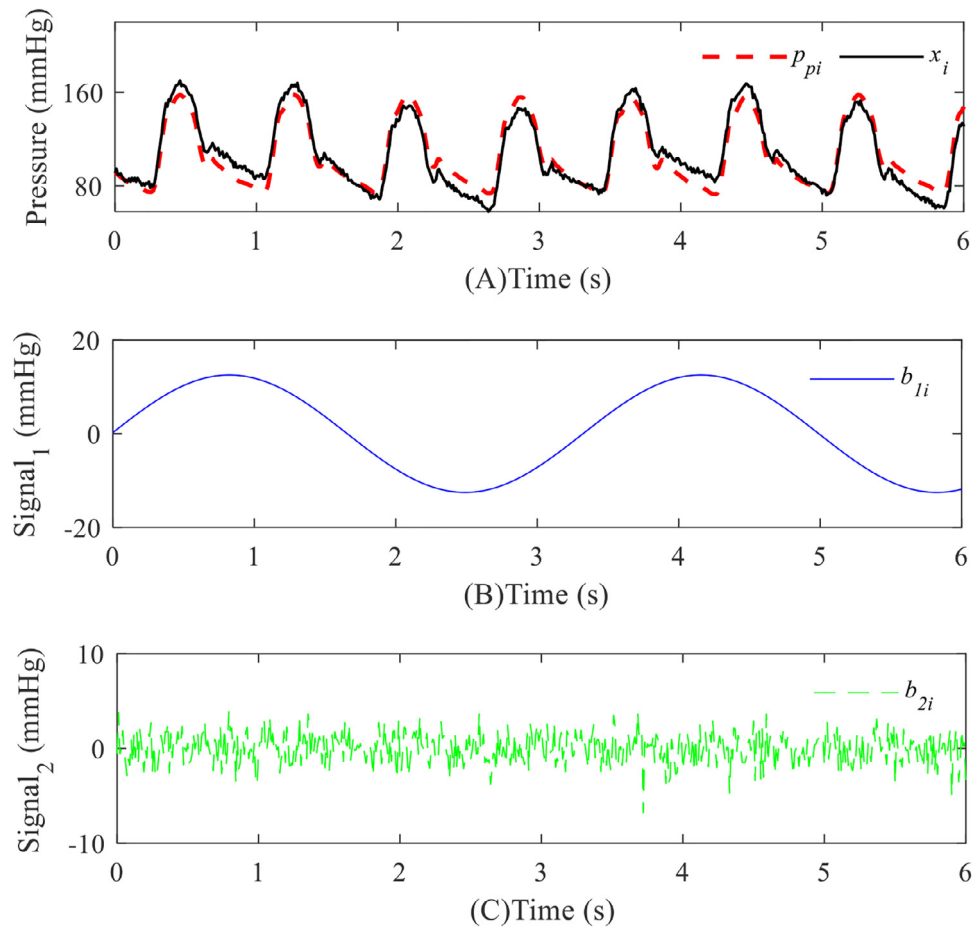


Fig. 1. Examples of a pulse wave, simulated baseline modulation and Gaussian random noise signals (SNR =25 dB). p_{pi} : pulse wave signal without noise; x_i : pulse wave signal with added Gaussian noise and respiratory modulation. b_{li} : simulated respiratory modulation signal; b_{2i} : Gaussian random noise signal.

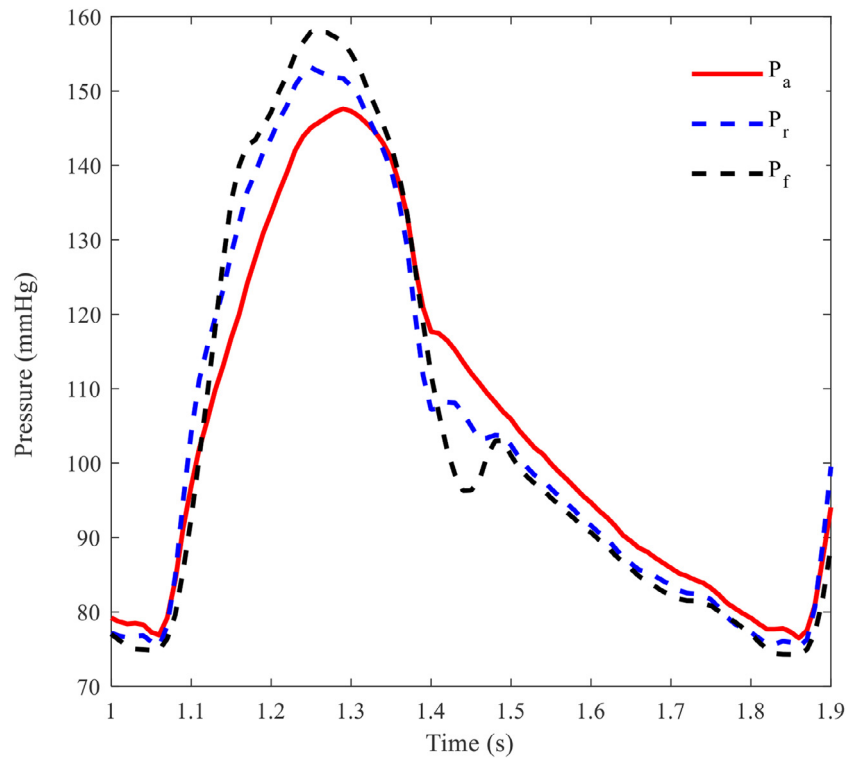


Fig. 2. Measured P_a and generated P_r and P_f waveforms using the FIR simulation model.

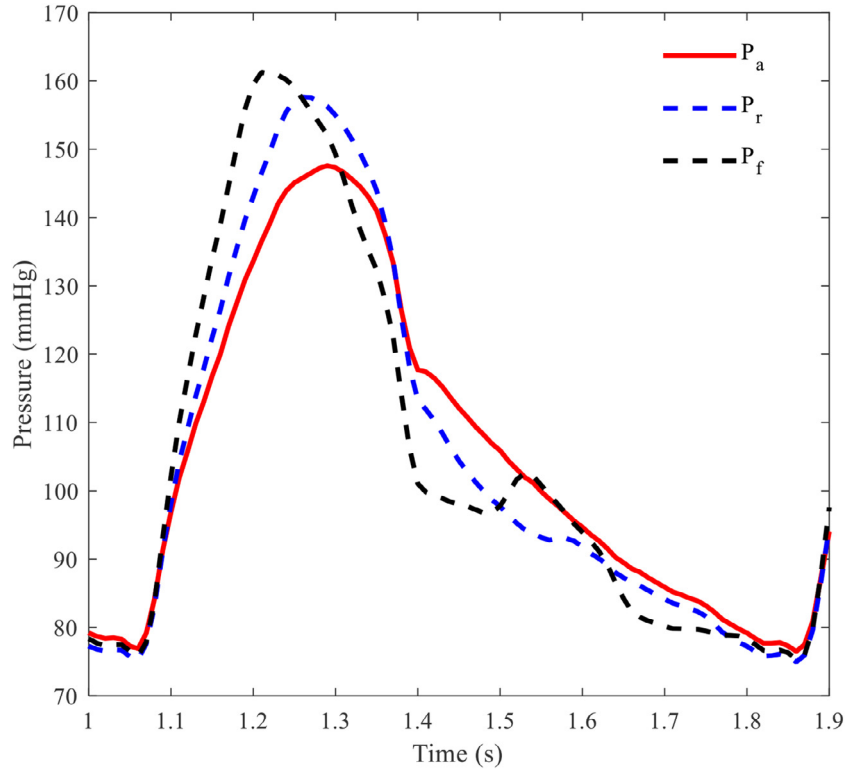


Fig. 3. An example of measured P_a waveform and the corresponding simulated P_r and P_f waveforms based on the tube-load model.

the output signals of two given FIRs with the above-mentioned P_a waveform as the input signal.

The impulse responses of the two channels, were as used in a previous study [20]. The FIR coefficients refer to the pressure signal transmission from the aorta to the upper and lower limb arteries, respectively.

2.1.2. Simulation data generated with the tube-load model

The ascending aortic to peripheral wave propagation path is modeled by a uniform lossless tube and a Windkessel load. This set up is usually called the tube-load model, the transfer function of which is given by:

$$G(z) = \frac{P_p(z)}{P_a(z)} = \frac{z^{N_a-p+1} + [(\eta_1 + \eta_2)/F_s - 1]z^{N_a-p}}{z^{2N_a-p+1} + (\eta_1/F_s - 1)z^{2N_a-p} + \eta_2/F_s} \quad (3)$$

Derivation of the equations and further details can be found in [14]. The transfer function of the tube-load model has three unknown parameters: $N_a - p$, η_1 and η_2 . In Eq. (4), Z_C represents the characteristic impedance of the tube, the terminal of which is composed of a Windkessel load consisting of the compliance (C_T) of the distal arteries and a peripheral resistance (R_T) due to the arterioles. Z_L represents the terminal impedance of the Windkessel load. In Eq. (5), $n_a - p$ is the pulse transit time associated with the wave propagation from the ascending aorta to the distal end of the cardiovascular system. F_s is the sampling frequency.

$$\eta_1 = \frac{2Z_C + R_T}{2Z_C \cdot R_T \cdot C_T}, \quad \eta_2 = \frac{R_T}{2Z_C \cdot R_T \cdot C_T} \quad (4)$$

$$N_a - p = n_a - p \cdot F_s, \quad N_L = 2N_a - p + 1 \quad (5)$$

In many previous studies, the tube-load model has been used in animals to estimate central aortic hemodynamics based on the relative ease of obtaining P_p waveforms [25,33,34,35]. The model has been rarely used in human subjects due to the difficulty of obtaining invasive aortic pressure measurements and simultaneous multiple peripheral artery pressures. In one such study [14], the values

of the physiologically relevant parameters of the tube-load model (load compliance, characteristic impedance, and peripheral resistance, pulse transit time etc.) were derived from the measured aortic blood pressure and estimated aortic blood pressure. The mean values of the parameters such as η_1 , η_2 and $n_a - p$ from this study [14] were used in this simulation. Their values are 94.6 and 16.6 for radial artery; and 82.5 and 40.6 for the femoral artery. The order N_L of the transfer function is determined by the values of the parameter $n_a - p$ for the upper and lower limbs. The $n_a - p$ of the upper and lower limbs were set to 86.9 ms and 64.4 ms, respectively. The same P_a waveform in Section 2.1.1 was also used as the input signal to the tube-load models. The simulated waveforms are shown in Fig. 3.

2.1.3. Animal experiments

Blood pressure in the ascending aorta, brachial and femoral arteries was recorded in two anesthetized Sprague-Dawley rats, weighing 0.32 kg and 0.35 kg. Blood pressures were measured simultaneously through three catheters, each connected to a transducer (MLT1199, AD Instruments, Castle Hill Australia). The catheters were introduced via incisions in the right common carotid artery and right brachial and left femoral arteries. The carotid catheter (outer diameter (o.d.) 0.90 mm and an inner diameter (i.d.) 0.50 mm.) was passed into the ascending aorta to record aortic pressure. For the brachial and femoral artery measurements, smaller catheters, o.d. 0.60 mm and i.d. 0.30 mm were used. A Power Lab 8/35 (PL3508) and quad Bio Amp (FE224) acquisition system (AD Instruments, Castle Hill Australia) and Lab Chart software running on a laptop computer were used for displaying and storing the data in real time, at a sampling rate of 1 kHz. All the animal experimental procedures were approved by the Institutional Animal Care and Use Committee (IACUC) of Shenzhen Institutes of Advanced Technology, Chinese Academy of Sciences: (SIAT-IACUC-190801-YGS-LWH-A0454-01).

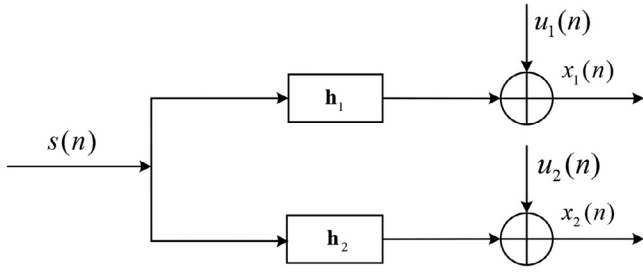


Fig. 4. Black-box structure of a two-channel FIR system.

2.2. Estimation of the P_a by the MBSI algorithm

In this study, the cardiovascular system is regarded as a black-box model of a two-channel wave propagation system, with one channel corresponding to the upper limb and the other to the lower limb. Up to now, many MBSI approaches have assumed the arterial system to be linear and short-time invariant [20]. Here, we present a method for P_a waveform estimation, with a FIR filter used as a transfer function. For a two-channel FIR system as presented in Fig. 4, $s(n)$ denotes the P_a waveform; $x_i(n)$, ($i = 1, 2$) denotes the P_p waveforms; the L -by-1 vector $\mathbf{h}_i = [h_i(0), h_i(1), \dots, h_i(L-1)]^T$, ($i = 1, 2$) represents the channel's impulse response between the P_a waveform and the i th P_p waveform; $u_i(n)$ is the additive noise.

A linear convolution between the P_a and P_p waveforms is then given by Eq. (6) [26]:

$$x_i(n) = \sum_{k=0}^{L-1} h_i(k)s(n-k) + u_i(n) \quad (6)$$

The two P_p waveforms are not independent; they conform to the so-called cross-relation (CR):

$$x_1(n)*h_2(n) = x_2(n)*h_1(n) + \theta_{12}(n) \quad (7)$$

where

$$\theta_{12}(n) = u_1(n)*h_2(n) - u_2(n)*h_1(n) \quad (8)$$

The $*$ symbol is the linear convolution operator. The cross-relation in Eq. (7) can be rewritten in matrix form as:

$$\mathbf{C}(n)\mathbf{h} + \theta_{12}(n) = 0 \quad (9)$$

where $\mathbf{C}(n) = [\mathbf{x}_2(n), -\mathbf{x}_1(n)]$; $\mathbf{h} = [\mathbf{h}_1^T, \mathbf{h}_2^T]^T$; $\mathbf{x}_i(n) = [x_i(n), x_i(n-1), \dots, x_i(n-L+1)]^T$.

2.2.1. An introduction to the SKF algorithm

For P_a waveform estimation, the first step is to identify the multichannel impulse response vector \mathbf{h} . Taking into account the cross-relation in Eq. (9), we propose the following Kalman filter problem for \mathbf{h} estimation. The process and measurement equations are given as follows: a) Process equation:

$$\mathbf{h}(n+1) = \mathbf{F}(n+1, n)\mathbf{h}(n) + \mathbf{v}_1(n) \quad (10)$$

b) Measurement equation:

$$\mathbf{y}(n) = \mathbf{C}(n)\mathbf{h}(n) + \mathbf{v}_2(n) \quad (11)$$

where the vectors $\mathbf{v}_1(n)$ and $\mathbf{v}_2(n) = \theta_{12}(n)$ denote the process and measurement noise, respectively; the state transition matrix is assumed to be $\mathbf{F}(n+1, n) = \mathbf{I}$ (identity matrix) because the cardiovascular system is a slow time-varying system; the observation vector $\mathbf{y}(n) = \mathbf{0}$ ($n = 1, 2, \dots, N$) is a zero-vector series. For the special transition matrix and the zero-observation vector, the computation of the Kalman filter is simplified as in Table 2.

As shown in Table 2, for the simplified multichannel identification problem, the correlation matrix of process noise is assumed

Table 2
Summary of the SKF algorithm.

Input vector process:
$x_1(n), x_2(n)$
Known parameters:
$\mathbf{F}(n+1, n) = \mathbf{I}$
$\mathbf{Q}_1(n) = 0, \mathbf{Q}_2(n) = \begin{cases} 10^{-7}\mathbf{I}, & \text{Noiseless} \\ \mathbf{I}, & \text{Noisy} \end{cases}$
Computation: $n = 1, 2, 3, \dots$
$\mathbf{G}(n) = \mathbf{K}(n-1)\mathbf{C}^T(n)[\mathbf{C}(n)\mathbf{K}(n-1)\mathbf{C}^T(n) + \mathbf{Q}_2(n)]^{-1}$
$\hat{\mathbf{h}}(n+1) = \hat{\mathbf{h}}(n) - \mathbf{G}(n)\mathbf{C}(n)\hat{\mathbf{h}}(n)$, here $\ \mathbf{h}\ _2 = 1$
$\mathbf{K}(n) = \mathbf{K}(n-1) - \mathbf{G}(n)\mathbf{C}(n)\mathbf{K}(n-1)$

to be $\mathbf{Q}_1(n) = 0$ (meaning $\mathbf{v}_1(n) = 0$) and the correlation matrix of the measurement noise is assumed to be $\mathbf{Q}_2(n)$. The matrix $\mathbf{G}(n)$ represents the Kalman gain, and the $\mathbf{K}(n)$ represents the filtered state-error correlation matrix.

2.2.2. Multichannel deconvolution algorithm

After the identifying the SIMO system using the SKF algorithm, the P_a waveform can be obtained by the deconvolution of the two known P_p waveforms. These deconvolution problems are of two types. First, if both the output signal and the channel responses are known, the input signal can be solved by ordinary deconvolution. Second, if only the output signal is known, both the input signal and the channel transfer function need to be solved. This second type is known as blind deconvolution and is more difficult to handle than ordinary deconvolution. Nevertheless, multichannel blind deconvolution algorithms have been used in many applications including signal processing [27], medical imaging [28] and seismic imaging [29]. Several blind deconvolution algorithms have been proposed, including the Sato algorithm [30], Godard algorithm [31] as well as Bussgang-type algorithms [32]. However, these algorithms require prior knowledge of the source statistics. The multi-input multi-output theorem can also be used to solve a multichannel inverse system and then to filter multiple signals [33]. In this paper, the channel responses are solved by the SKF algorithm. Both two-channel output signals and the corresponding two FIRs are known and used to solve the common input signal based on a multichannel least squares deconvolution. Eq. (6) can be rewritten in matrix form:

$$\begin{bmatrix} \mathbf{x}_1 \\ \mathbf{x}_2 \end{bmatrix} = \begin{bmatrix} \mathbf{H}_1 \\ \mathbf{H}_2 \end{bmatrix} \mathbf{s} + \begin{bmatrix} \mathbf{u}_1 \\ \mathbf{u}_2 \end{bmatrix} \quad (12)$$

where

$$\mathbf{x}_i = [x_i(0), x_i(1), \dots, x_i(N-1)]^T \quad (13)$$

$$\mathbf{u}_i = [u_i(0), u_i(1), \dots, u_i(N-1)]^T \quad (14)$$

$$\mathbf{s} = [s(-L+1), s(-L+2), \dots, s(N-1)]^T \quad (15)$$

and N denotes the number of the measured P_p waveform samples.

$$\mathbf{H}_i = \begin{bmatrix} h_i(L-1) & \dots & h_i(0) & \dots & \dots & 0 \\ 0 & h_i(L-1) & \dots & h_i(0) & \dots & 0 \\ \dots & \dots & \dots & \dots & \dots & \dots \\ 0 & \dots & \dots & h_i(L-1) & \dots & h_i(0) \end{bmatrix} \quad (16)$$

Here \mathbf{H}_i is the $[N \times (N+L-1)]$ Toeplitz matrix composed of the estimated impulse responses of the channel. The linear least squares solution of the problem is given by:

$$\mathbf{s} = (\mathbf{H}^T \mathbf{H})^{-1} \mathbf{H}^T \mathbf{x} \quad (17)$$

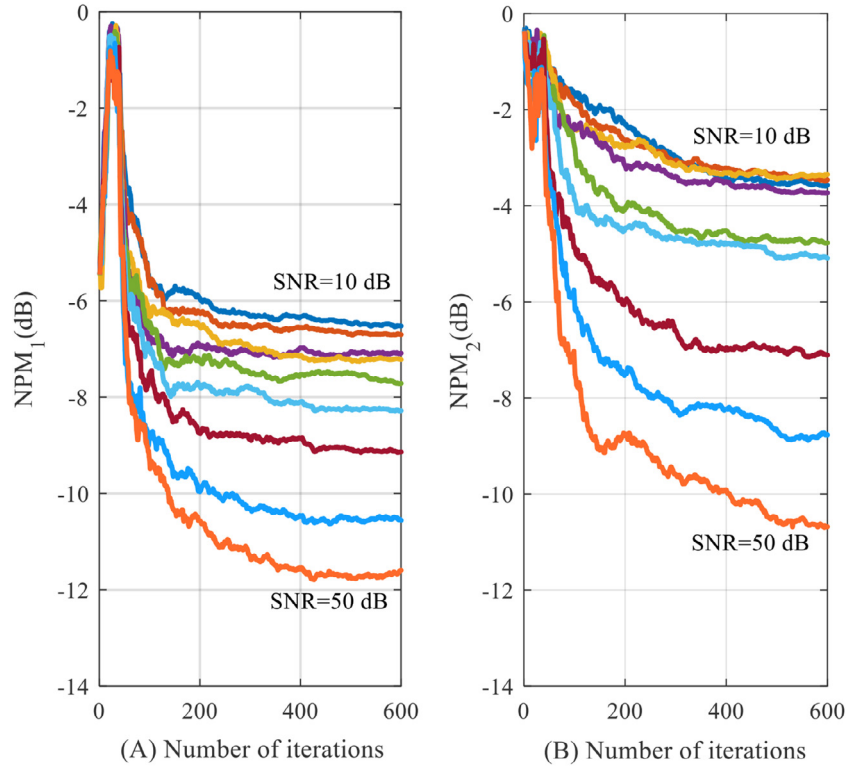


Fig. 5. The convergence behavior of averaged NPMs at different SNRs for each channel in a two-channel system.

where

$$\mathbf{H} = [\mathbf{H}_1^T, \mathbf{H}_2^T]^T \quad (18)$$

$$\mathbf{x} = [\mathbf{x}_1^T, \mathbf{x}_2^T]^T \quad (19)$$

2.2.3. Evaluation and statistical analysis

In all experiments, we used the root mean square error (RMSE) as a measure of the quality of the quantitative assessments. RMSE is defined as follows:

$$\text{RMSE} = \sqrt{\frac{1}{N} \sum_{n=1}^N [s(n) - \hat{s}(n)]^2} \quad (20)$$

In Eq. (20), $s(n)$ is the real source input signal for the system identification; $\hat{s}(n)$ is the estimated source input signal and N represents the total number of data points comprising the test signal.

Normalized projection misalignment (NPM) is commonly used to evaluate the convergence performance of the estimated impulse responses in blind SIMO systems [36,37]. The NPM is computed during the iteration process and is given by:

$$\text{NPM}_i(k) = 20 \log_{10} \frac{\|\mathbf{h}_i - \frac{\hat{\mathbf{h}}_i^T \hat{\mathbf{h}}_i(k)}{\hat{\mathbf{h}}_i^T(k) \hat{\mathbf{h}}_i(k)} \hat{\mathbf{h}}_i(k)\|}{\|\hat{\mathbf{h}}_i\|} \quad (21)$$

where $\|\cdot\|$ is the l_2 norm; k is the iteration index; \mathbf{h}_i and $\hat{\mathbf{h}}_i$ are the real and estimated FIRs, respectively.

Measured and estimated central aortic pressures are reported as mean \pm SD or 95% CI where appropriate. Differences between them were analyzed by a paired t -test (IBM SPSS Statistics, version-23). The linear regression parameters and Pearson's correlation coefficients between the measured and estimated central aortic pressure were also calculated. Bland-Altman plots were constructed to assess the agreement between estimated and measured

central aortic pressure. A p -value smaller than 0.01 was considered to be statistically significant.

3. Results

3.1. FIR simulation experiments

Blind system identification algorithms are usually sensitive and vulnerable to measurement noise [21]. The SNR of the observed output signals can affect the convergence process and the noise of each channel is unknown in practice. Therefore, simulation experiments were conducted to verify the performance of the proposed algorithm under a range of different SNRs. In Fig. 5, the curves represent the convergence performance of the SKF algorithm when applied to signals with various SNRs, with each panel representing one channel. The curves from top to bottom correspond to SNRs from 10 dB to 50 dB. Fig. 6 shows the effect of iteration number on the relationship between RMSE and SNR, using the SKF algorithm. As shown in the figure, the number of iterations is in the range 80 to 200.

All simulation results are summarized in Table 3. To simulate real *in vivo* measurements where noise is inevitable, we applied the proposed SKF and CCA algorithms to estimate the P_a waveform by adding noise to P_p to produce a SNR of 25 dB. The RMSEs of the measured and estimated P_a were computed for the total waveform (TW), SP and beat-to-beat diastolic pressure (DP). For a SNR of 25 dB (shown in bold), it can be seen that the TW RMSE of the measured and estimated P_a waveforms using the CCA algorithm is 6.43 ± 2.66 mmHg, whereas the corresponding value obtained from the SKF algorithm is 3.31 ± 1.92 mmHg.

The two algorithms were compared by a paired t -test. The SKF algorithm has significantly lower RMSEs than the CCA up to a SNR of 40 dB to 45 dB. Fig. 7 shows that there was a significant difference between the CCA and SKF methods when the SNR values were less than 35 dB ($p < 0.01$), although not for SNR val-

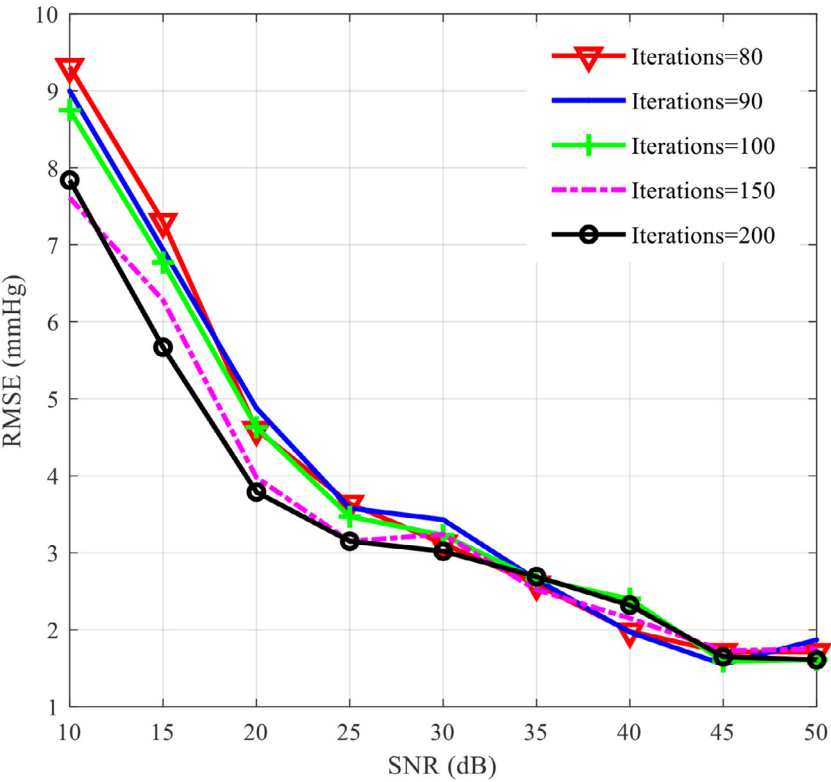


Fig. 6. Effect of iteration number on the relationship between RMSE and SNR, using the SKF algorithm.

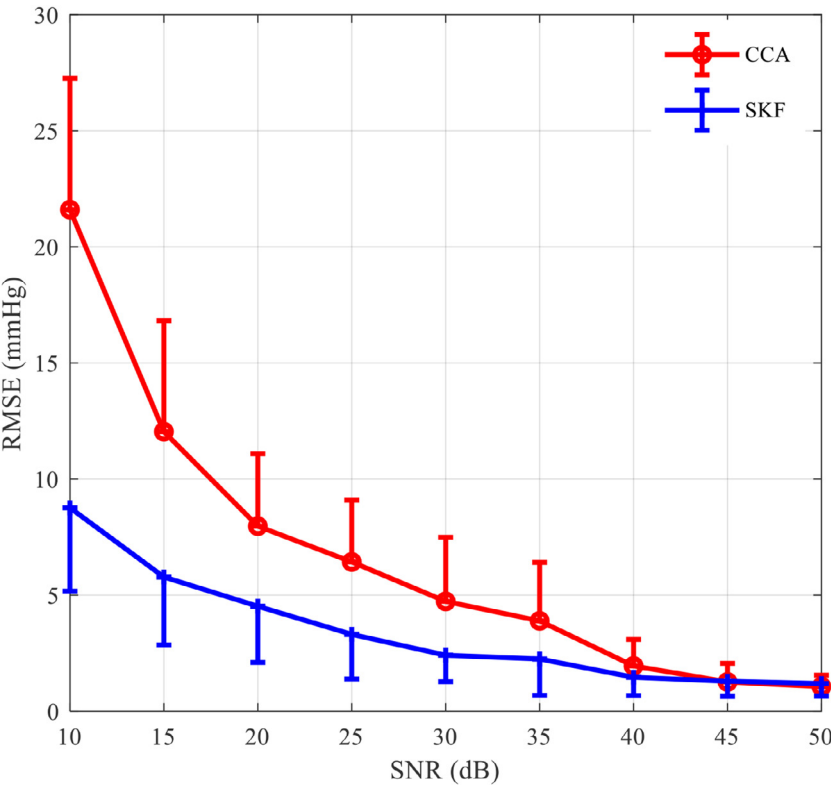


Fig. 7. Effect of added noise on the RMSE values obtained from measured and estimated P_a waveforms using the CCA and SKF algorithms (Mean \pm SD, the number of points in the total waveform, n is 600).

Table 3

RMSEs obtained from measured and estimated P_a waveforms using the CCA and SKF algorithms at different added noise levels (Mean \pm SD).

SNR(dB)	Method	TW(mmHg)	SP(mmHg)	DP(mmHg)
10	CCA	21.60 \pm 5.66	30.9 \pm 12.95	143.36 \pm 106.56
	SKF	8.76 \pm 3.59	5.28 \pm 2.26	13.11 \pm 9.94
15	CCA	12.04 \pm 4.78	13.45 \pm 7.61	55.55 \pm 40.98
	SKF	5.78 \pm 2.93	2.46 \pm 1.45	3.46 \pm 2.33
20	CCA	7.97 \pm 3.12	5.38 \pm 2.00	11.43 \pm 9.03
	SKF	4.52 \pm 2.42	1.44 \pm 0.78	1.55 \pm 0.90
25	CCA	6.43 \pm 2.66	2.27 \pm 0.97	3.16 \pm 1.73
	SKF	3.31 \pm 1.92	0.93 \pm 0.42	1.12 \pm 0.58
30	CCA	4.73 \pm 2.76	1.16 \pm 0.56	1.55 \pm 0.91
	SKF	2.41 \pm 1.14	0.77 \pm 0.22	0.99 \pm 0.43
35	CCA	3.89 \pm 2.52	0.78 \pm 0.24	1.03 \pm 0.45
	SKF	2.25 \pm 1.57	0.77 \pm 0.27	0.89 \pm 0.30
40	CCA	1.95 \pm 1.14	0.77 \pm 0.23	0.87 \pm 0.32
	SKF	1.46 \pm 0.79	0.76 \pm 0.22	0.81 \pm 0.21
45	CCA	1.26 \pm 0.80	0.75 \pm 0.23	0.80 \pm 0.20
	SKF	1.29 \pm 0.65	0.74 \pm 0.22	0.79 \pm 0.18
50	CCA	1.06 \pm 0.49	0.75 \pm 0.22	0.76 \pm 0.19
	SKF	1.19 \pm 0.54	0.75 \pm 0.22	0.76 \pm 0.22

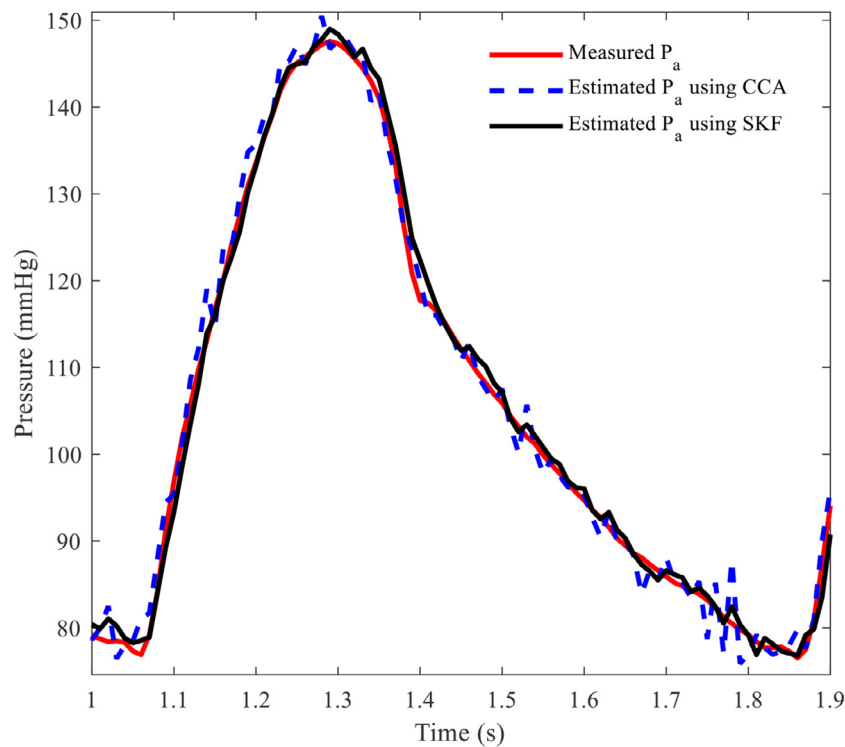


Fig. 8. Measured and estimated P_a waveforms using the CCA and SKF algorithms from the same subject for a SNR of 25 dB.

ues greater than 35 dB ($p > 0.01$). In general, the results show that the SKF method is more noise-tolerant than the CCA method. Fig. 8 compares the measured and estimated P_a waveforms using the CCA and SKF algorithms, operating on the same FIR simulation dataset. The correlation between the measured and estimated pressures is shown in Figs. 9(A) and 10(A) for the CCA and SKF algorithms, respectively. Also shown in each plot are the line of identity and the equation of the linear fit to the data. Figs. 9(B) and 10(B) are the corresponding Bland-Altman plots in which the mean bias is shown by the solid horizontal line and limits of agreement ($\pm 1.96SD$ of the mean difference), by dashed lines.

The linear regression equations obtained between the measured and estimated P_a waveforms using the CCA and SKF algorithms were $y = 1.00x - 0.14$ ($r = 0.99$, $p < 0.01$) in Fig. 9(A) and $y = 1.00x + 0.28$ ($r = 0.99$, $p < 0.01$) in Fig. 10(A). A comparison

(mean \pm SD, -0.11 ± 2.27 mmHg) between the measured and estimated P_a waveforms using the CCA algorithm is shown in Fig. 9(B); and a similar comparison using the MCN algorithm (mean \pm SD, -0.10 ± 1.80 mmHg) is shown in Fig. 10(B).

3.2. Tube-load modeling of arterial pressure waveforms in human subjects

As shown in Fig. 11, the SKF algorithm also has significantly lower RMSEs than the CCA. The proposed SKF algorithm clearly outperforms the CCA algorithm ($p < 0.01$). It is notable that, as shown in Fig. 11, the RMSE values of the measured and estimated P_a waveforms using the CCA algorithm are more than 5 mmHg for all values of SNR investigated. Thus, the mean difference between the estimated and measured P_a waveforms does not satisfy

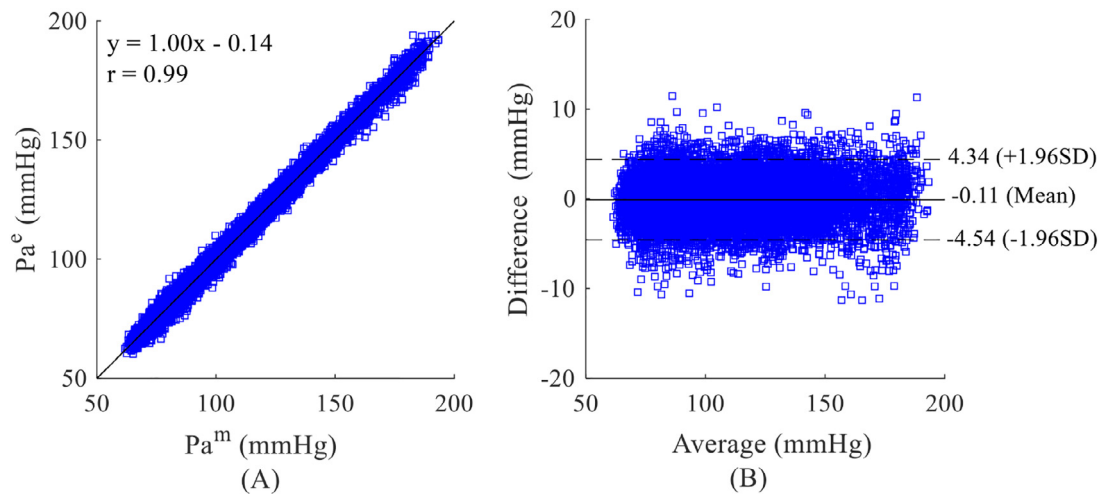


Fig. 9. (A) Correlation analysis and (B) Bland-Altman plots comparing measured and estimated P_a waveforms for a SNR of 25 dB using the CCA algorithm and FIR simulation data (25 subjects). P_a^m and P_a^e are the measured and estimated pressures, respectively.

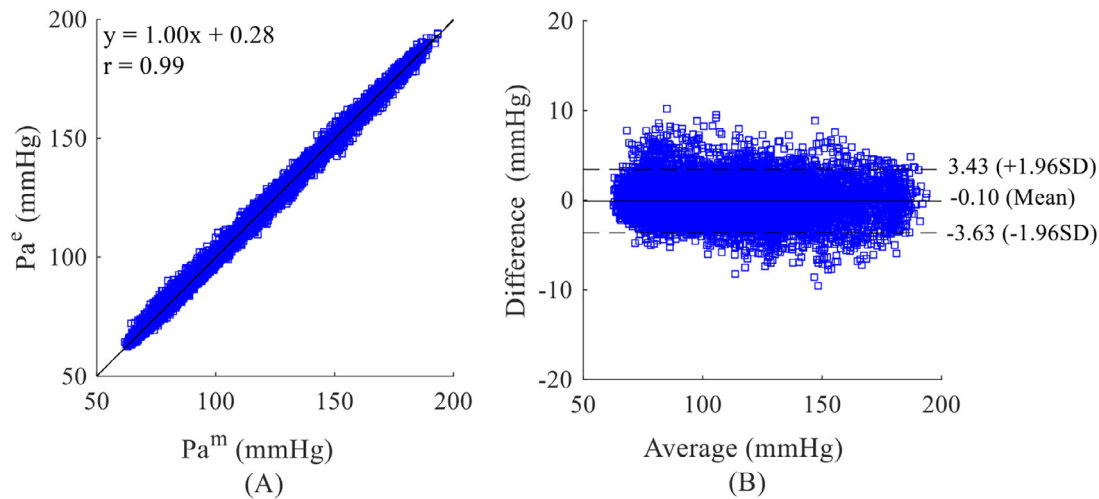


Fig. 10. (A) Correlation analysis and (B) Bland-Altman plots comparing measured and estimated P_a waveforms for a SNR of 25 dB using the SKF algorithm and FIR simulation data (25 subjects). P_a^m and P_a^e are the measured and estimated pressures, respectively.

the Association for the Advancement of Medical Instrumentation standard of 5 ± 8 mmHg [38,39], whereas this requirement is met by the SKF approach, for SNRs of 25 dB and above. Again, a SNR of 25 dB, corresponding to a typical real-world value, has been used in Fig. 12 to provide a visual comparison of the performance of the two algorithms, where it is seen that the qualitative agreement between measured and estimated waveforms is good for the SKF algorithm but clearly inferior for the CCA approach.

Considering the tube-load simulation experiments, Table 4 shows that for SNRs greater than 25 dB there is little change in the RMSEs for SP and DP when calculated by either algorithm, although the SKF values remained consistently lower.

When the SNR increases from 10 dB to 40 dB, the corresponding RMSE values for TW continue to decrease, as also listed in Table 4. Point-by-point comparisons of the pressure signals analyzed by the CCA and SKF algorithms are shown in the correlation plots of Figs. 13(A) and 14(A). Also, in each plot the line of identity and the equation of the linear fit to the data are shown. Figs. 13(B) and 14(B) are the corresponding Bland-Altman plots in which the mean bias is shown by the solid horizontal line and limits of agreement (± 1.96 SD of the mean difference), by dashed lines. The superior performance of the SKF approach is evident in the higher value of the Pearson correlation coefficient ($r = 0.99$,

Table 4

RMSE values obtained from measured and estimated P_a waveforms using the CCA and SKF algorithms with the different SNRs of the observed channel output signals (Mean \pm SD).

SNR (dB)	Method	TW (mmHg)	SP (mmHg)	DP (mmHg)
10	CCA	22.39 ± 6.80	36.79 ± 11.91	122.09 ± 62.58
	SKF	7.59 ± 3.12	3.41 ± 2.35	4.10 ± 4.60
15	CCA	10.95 ± 3.27	16.57 ± 6.02	31.45 ± 30.11
	SKF	5.19 ± 1.52	3.19 ± 1.79	1.70 ± 0.67
20	CCA	8.03 ± 3.04	11.01 ± 5.03	9.02 ± 5.10
	SKF	4.60 ± 1.87	2.24 ± 1.47	1.24 ± 0.74
25	CCA	7.03 ± 2.15	8.77 ± 4.85	2.87 ± 1.67
	SKF	4.43 ± 2.05	2.16 ± 1.57	0.96 ± 0.61
30	CCA	6.74 ± 2.12	8.34 ± 5.00	1.72 ± 1.55
	SKF	4.49 ± 2.12	2.83 ± 2.45	0.82 ± 0.73
35	CCA	6.76 ± 2.16	8.23 ± 4.93	1.33 ± 1.09
	SKF	4.71 ± 1.96	4.15 ± 3.66	0.64 ± 0.42
40	CCA	7.10 ± 2.64	8.38 ± 5.09	1.34 ± 1.03
	SKF	4.68 ± 1.81	3.60 ± 3.50	0.72 ± 0.35
45	CCA	6.98 ± 2.39	8.33 ± 5.08	1.22 ± 1.05
	SKF	4.63 ± 1.79	3.20 ± 3.27	0.81 ± 0.44
50	CCA	6.77 ± 1.97	8.24 ± 4.97	1.14 ± 1.08
	SKF	4.66 ± 2.30	2.84 ± 2.60	0.98 ± 0.73

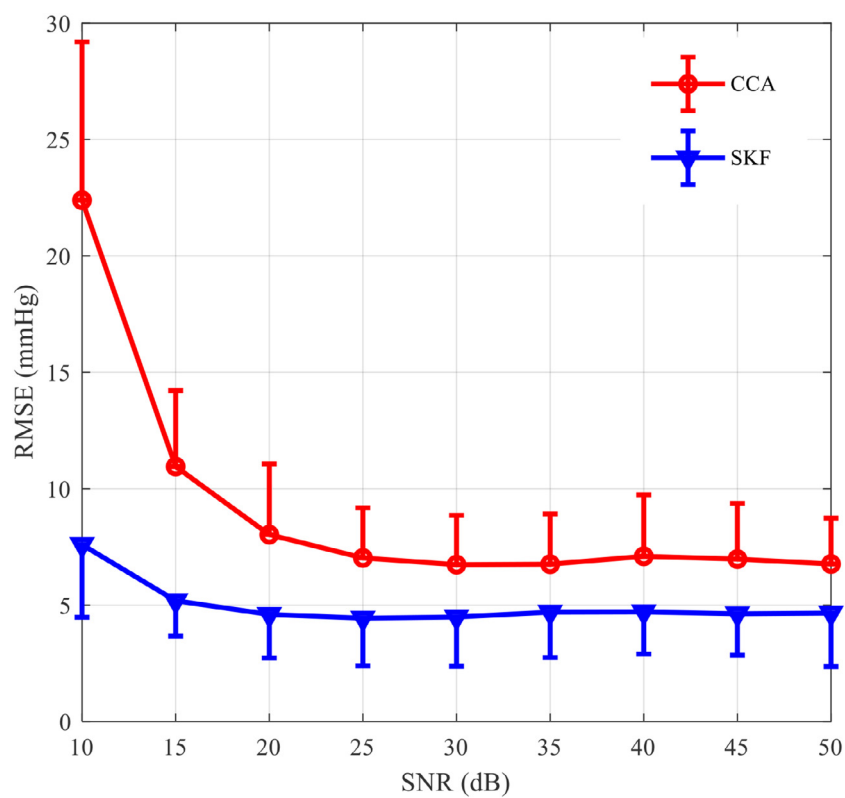


Fig. 11. Effect of added noise on the RMSE values obtained from the measured and estimated P_a waveforms, using the CCA and SKF algorithms (Mean \pm SD, the number of points in the total waveform, n is 600).

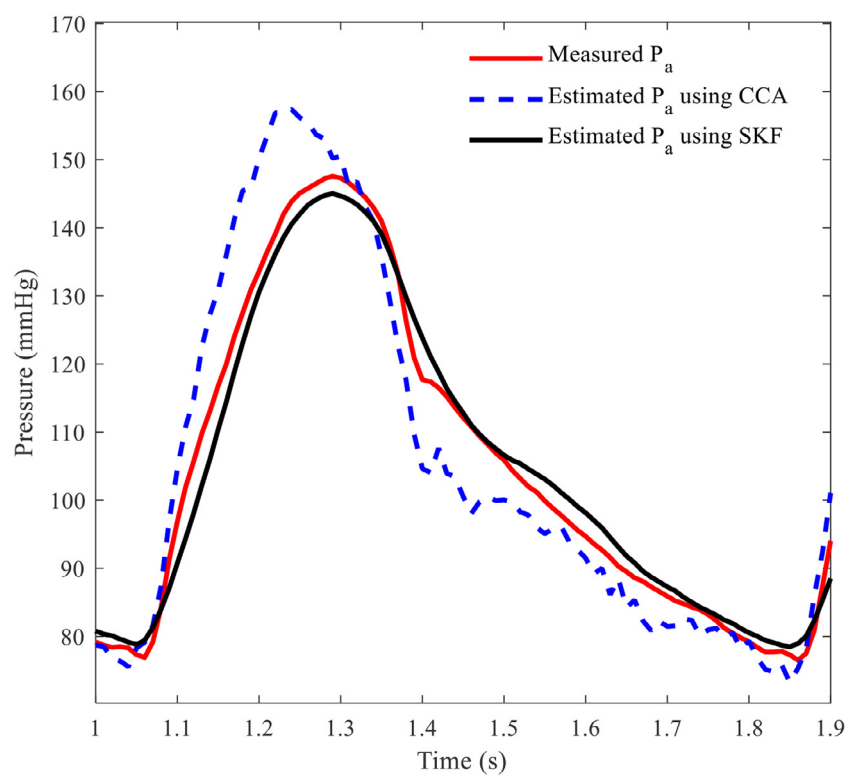


Fig. 12. Measured and estimated P_a waveforms using the CCA and SKF algorithms from the same subject for a SNR of 25 dB.

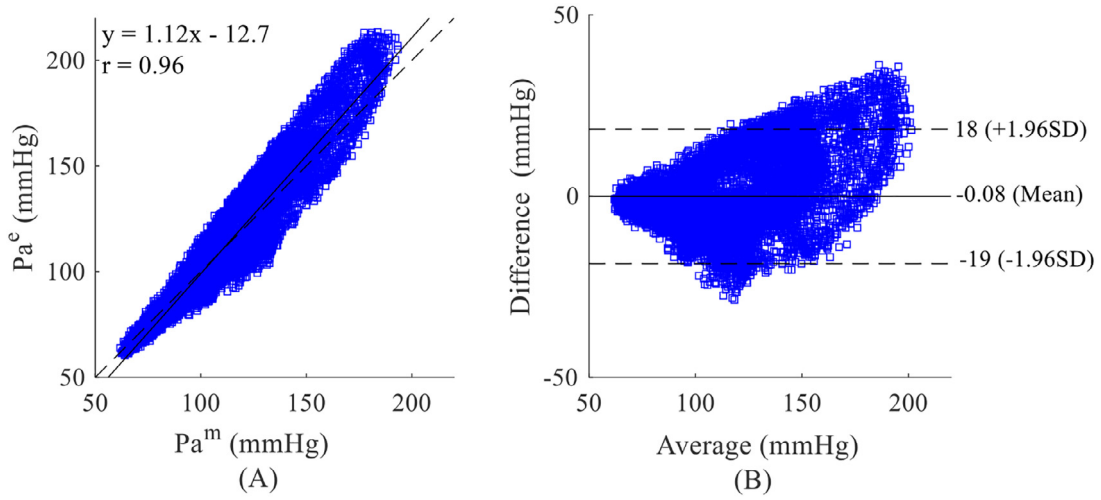


Fig. 13. (A) Correlation analysis and (B) Bland-Altman plots comparing measured and estimated P_a waveforms for a SNR of 25 dB using the CCA algorithm and FIR simulation data (25 subjects). P_a^m and P_a^e are the measured and estimated pressures, respectively.

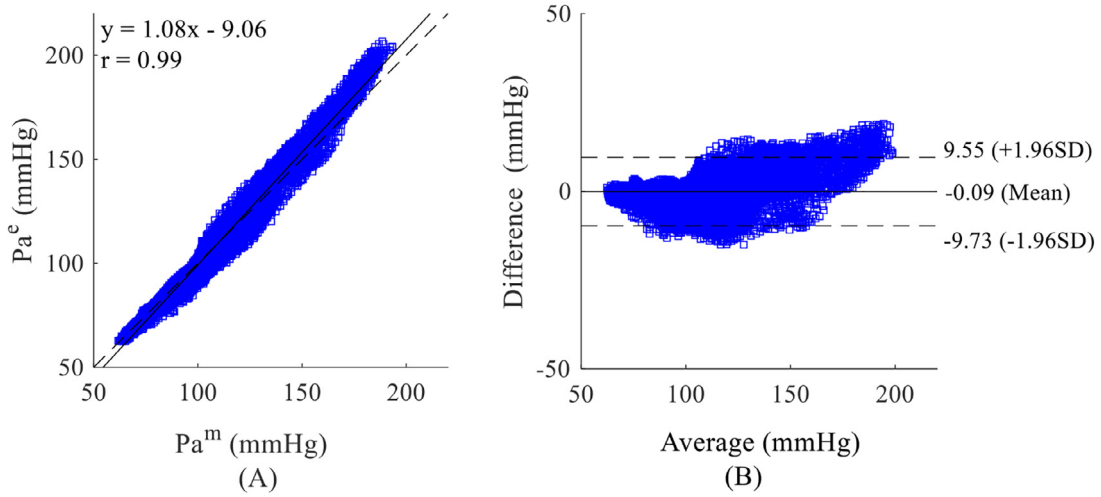


Fig. 14. (A) Correlation analysis and (B) Bland-Altman plots comparing measured and estimated P_a waveforms for a SNR of 25 dB using the SKF algorithm and FIR simulation data (25 subjects). P_a^m and P_a^e are the measured and estimated pressures, respectively.

$p < 0.01$ vs. $r = 0.96$, $p < 0.01$) and the narrower limits of agreement (± 9.73 mmHg vs. ± 19 mmHg).

3.3. Animal experiments

To verify the accuracy and effectiveness of the proposed SKF algorithm *in vivo*, we performed measurement on two Sprague-Dawley rats. The channel order was assumed to be 20 and the number of points in the total waveform of every sample was 1800. The estimated and true pressure waveforms agreed well. The average RMSE of the total waveform between the measured and estimated P_a waveforms using the SKF algorithm was 1.20 mmHg and that using the CCA algorithm, 1.70 mmHg.

The point-by-point correlation and corresponding Bland Altman plots (Figs. 15 and 16) again show that the SKF algorithm yields a higher correlation coefficient ($r = 0.99$, $p < 0.01$ vs. $r = 0.97$, $p < 0.01$) as well as narrower limits of agreement (± 3.29 mmHg vs. ± 6.50 mmHg). Fig. 17 is a direct comparison of the two algorithms and shows that the estimated P_a waveform using the SKF algorithm is closer to the measured P_a waveform than that obtained from the CCA algorithm, most notably near end systolic and end diastolic pressure.

4. Discussion

In this study, we have applied a simplified Kalman filter algorithm to estimate central P_a in simulations and *in vivo* experiments and compared the results to those obtained from the previously described CCA approach. In the simulations, we have shown that, although the results are similar at high SNRs, when the signal becomes relatively weaker the SKF algorithm outperforms the CCA algorithm. Furthermore, the proposed SKF algorithm for central P_a estimation does not require any explicit calibration as the method is by nature self-calibrating and can thus account for any inter-subject or intra-subject variability in vascular dynamics. The computational times of the CCA and SKF methods were 44.4 ms and 51.4 ms, respectively. The CCA approach uses matrix eigenvalue decomposition to directly solve eigenvectors as the response of the blind system, whereas the SKF method uses continuous updating iteratively to solve the response of blind system. Although the SKF method requires more time than the CCA approach, its accuracy is superior. As shown in Fig. 7, the RMSEs of the SKF method are smaller than those obtained when using the CCA approach.

In the simulation experiments, the convergence performance of the SKF algorithm has shown that the NPM values decrease

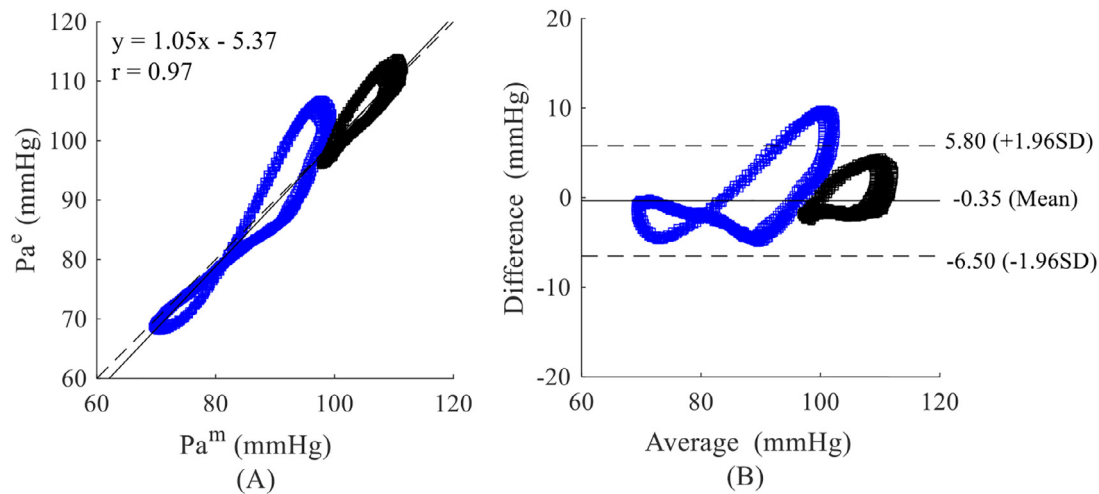


Fig. 15. (A) Correlation analysis and (B) Bland-Altman plots comparing measured and estimated P_a waveforms using the CCA algorithm (2 Sprague-Dawley rats). Animal₁, blue points; animal₂, black points. P_a^m and P_a^e are the measured and estimated pressures, respectively.

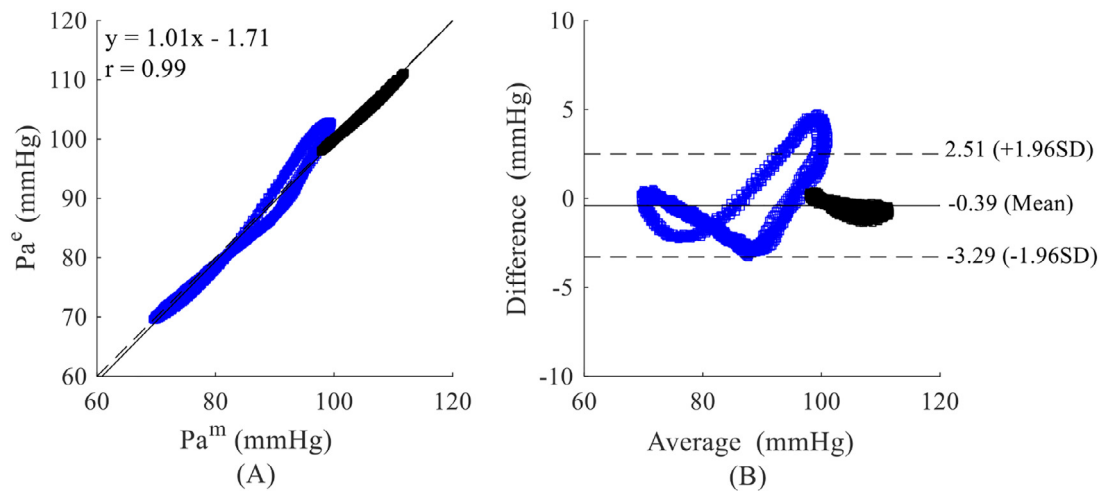


Fig. 16. (A) Correlation analysis and (B) Bland-Altman plots comparing measured and estimated P_a waveforms using the SKF algorithm (2 Sprague-Dawley rats).

markedly as the SNR increases. The convergence is fast and the channel impulse responses are accurately estimated when the SNR is high, as shown in Fig. 5. The results also demonstrate that the RMSEs decrease as the number of iterations increases, as shown in Fig. 6, where the number of iterations ranges from 80 to 200. It was found that if the number of iterations is less than the number of sampling points in one complete cardiac cycle, the P_a waveform cannot be reliably reproduced. Therefore, the number of iterations was maintained at a value not less than 80. For lower values of SNR, RMSEs fall with increasing number of iterations; although for SNRs greater than 30 dB, increasing the number of iterations had little further effect. Fig. 6 also shows that there is a small additional gain in performance when the number of iterations is increased from 150 to 200, the effect being more marked for low SNRs. These results indicate that the proposed SKF algorithm has a good overall performance when the number of iterations is 150 or more. Accordingly, to optimize the speed and accuracy in estimating the P_a waveform, the number of iterations of the SKF algorithm was set to 200. On the whole, TW RMSEs of the measured and estimated P_a waveforms using the SKF algorithm are lower than those seen when using the CCA algorithm. Moreover, the SKF algorithm gives lower RMSE values for SP and DP, as shown in

Tables 3 and 4. For the animal experiments, although the proposed SKF algorithm outperforms the CCA method, only two animals were measured, so this result should be regarded only as preliminary. Ideally, primates would be the experimental model in a study of this type because of their similarity to humans in physiology, neuroanatomy, reproduction, development, cognition, and social complexity. However they are not often used for cost and ethical reasons [41]. Pigs and humans share many physiological and anatomical similarities for organs such as skin, brain and, especially, the cardiovascular system. Therefore they have been widely used as experimental models [42]. Nevertheless, rats account for the majority of animal experiments and have yielded a large body of experimental data over many years. More importantly, rats and humans suffer from many of the same diseases, because they have the same basic physiology, similar organs, and similar body plans [43]. Furthermore they are robust and tolerate surgical procedures and anesthesia well. Therefore, in this preliminary study, rats were selected, with the intention of using pigs for further verification before applying the method in a clinical validation study on human subjects.

This study has a few limitations which will be addressed in future work. The morphology of the pulse waveform changes with

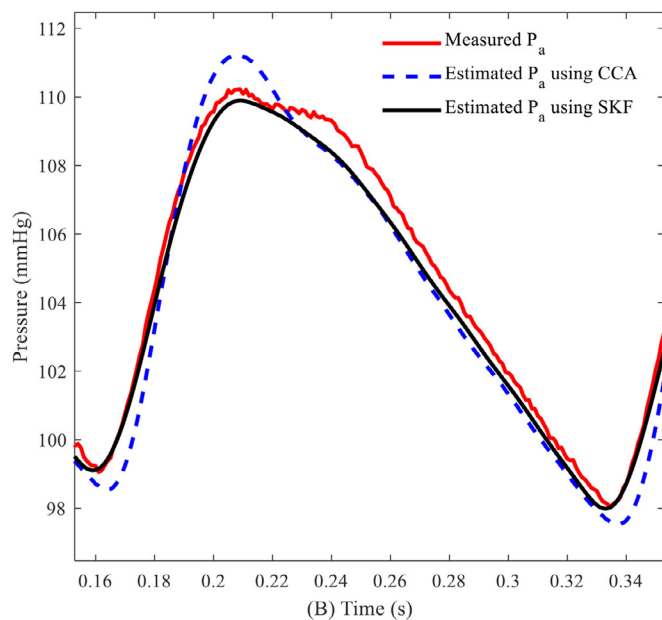
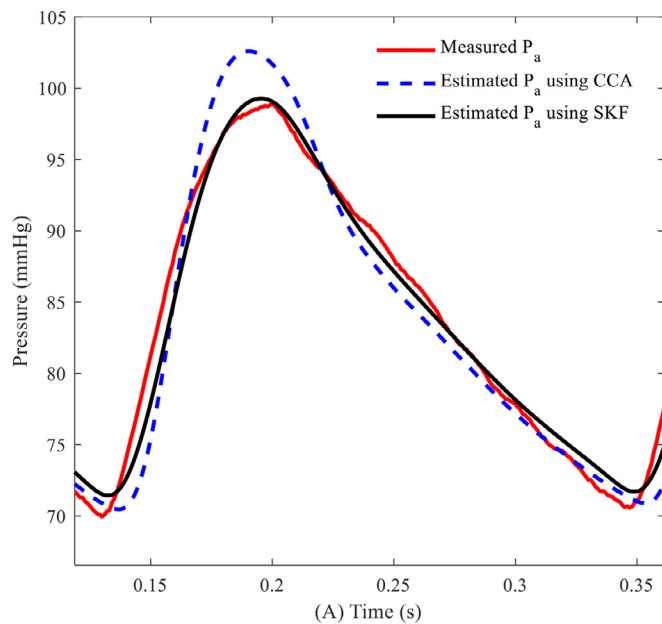


Fig. 17. Measured and estimated P_a waveforms using the CCA and SKF algorithms from 2 Sprague-Dawley rats (A and B).

position in the vascular tree, gender, age, cardiovascular disease etc [44–48]. The number of participants was small and most were female. In future work more volunteers will be recruited from subjects with cardiovascular pathology and the results will be compared with age- and sex-matched healthy controls. Although the aortic and brachial blood pressure measurements in our previous study were collected simultaneously, we did not record any additional peripheral pressures at the same time. The nonlinearity of the cardiovascular system is neglected, which may lead to some estimation errors in the timing of the systolic shoulder and the pressure at which it occurs, both of which will affect clinically important hemodynamic variables such as augmentation index, reflection magnitude and reflection index. Similar errors in the time and the pressure at which the dicrotic notch appears may also occur.

5. Conclusion and future work

The results of the simulation experiments demonstrate that the performance of MBSI algorithms based on the proposed SKF approach is superior to that of the CCA method over a wide range of SNRs in the observed signal. The results of the animal experiments also confirm that the proposed SKF algorithm is superior to the CCA algorithm. It is worth noting that the SKF algorithm is especially effective for estimating systolic and diastolic pressures, which from the clinician's point of view, as a measure of cardiac load, is of particular value. In a future study, we will measure more animals for the *in vivo* validation of the SKF approach. We also plan to develop a nonlinear blind identification algorithm as an alternative approach to the estimation of central pressure from peripheral measurements. The clinical data will be used to verify the proposed method. Improved accuracy in estimating central pressures from peripheral arterial pressure waveforms will provide a valuable step towards dependable measurement of the elusive but clinically important central aortic pressure waveform, particularly the pulse pressure, as an aid to the early diagnosis of cardiovascular disease.

Declaration of Competing Interest

The authors declare that they have no conflict of interests.

Acknowledgments

This work was supported by the National Key Research and Development Program of China (No. 2017YFC1307600), the Natural Science Foundation of Liaoning Province (No. 20170540312 and No. 2021-YGJC-14), the Basic Scientific Research Project (Key Project) of Liaoning Provincial Department of Education (LJKZ00042021), the National Natural Science Foundation of China (No. 61773110), and the Fundamental Research Funds for the Central Universities (No. N2119008). This research was also supported by the Shenyang Science and Technology Plan Fund (No. 21-104-1-24, No. 20-201-4-10, and No. 201375), the Member Program of Neusoft Research of Intelligent Healthcare Technology, Co. Ltd. (No. MCMP062002).

References

- [1] W. Bryan, et al., ESC/ESH Guidelines for the management of arterial hypertension: the task force for the management of arterial hypertension of the European Society of Cardiology (ESC) and the European Society of Hypertension (ESH), *Eur. Heart J.* 39 (33) (2018) 3021–3104 2018.
- [2] P. Salvi. *Pulse Waves*. Springer International Publishing, 2nd ed. 2017.
- [3] W.W. Nichols et al., McDonald's Blood Flow In Arteries: Theoretical, Experimental and Clinical Principles, in Hodder Arnold, 6th ed. London, 2011.
- [4] A.P. Avolio, et al., Arterial blood pressure measurement and pulse wave analysis—their role in enhancing cardiovascular assessment, *Physiol. Meas.* 31 (1) (Jan. 2009) 1–47.
- [5] W.W. Nichols, et al., Effects of arterial stiffness, pulse wave velocity, and wave reflections on the central aortic pressure waveform, *J. Clin. Hypertens.* 10 (4) (Apr. 2008) 295–303.
- [6] M.J. Roman, et al., Relations of central and brachial blood pressure to left ventricular hypertrophy and geometry: the strong heart study, *J. Hypertens.* 28 (2) (Feb. 2010) 384–388.
- [7] C.M. Mceniery, et al., Central blood pressure: current evidence and clinical importance, *Eur. Heart J.* 35 (26) (Jul. 2014) 1719–1725.
- [8] T.Y. Cai, et al., Central blood pressure in children and adolescents: non-invasive development and testing of novel transfer functions, *J. Hum. Hypertens.* 31 (12) (Aug. 2017) 831–837.
- [9] C.H. Chen, et al., Validation of carotid artery tonometry as a means of estimating augmentation index of ascending aortic pressure, *Hypertension* 27 (2) (Feb. 1996) 168–175.
- [10] R. Kelly, et al., Noninvasive carotid pressure wave registration as an indicator of ascending aortic pressure, *J. Vasc. Med. Biol.* 1 (Jan. 1989) 241–247.
- [11] F. Michael, et al., Noninvasive studies of central aortic pressure, *Curr. Hypertens. Rep.* 14 (1) (Feb. 2012) 8–20.
- [12] Y.T. Shih, et al., Quantification of the calibration error in the transfer function-derived central aortic blood pressures, *Am. J. Hypertens.* 24 (12) (Aug. 2011) 1312–1317.
- [13] G. Zhang, et al., Tube-load model parameter estimation for monitoring arterial hemodynamics, *Front. Physiol.* 2 (72) (Nov. 2011) 1–18.

- [14] M. Rashedi, et al., Comparative study on tube-load modeling of arterial hemodynamics in humans, *J. Biomech. Eng.* 135 (3) (Mar. 2013) 1–9.
- [15] O. Narayan, et al., Estimation of central aortic blood pressure, *J. Hypertens.* 32 (9) (Jun. 2014) 1727–1740.
- [16] Y.T. Shih, et al., Comparison of two generalized transfer functions for measuring central systolic blood pressure by an oscillometric blood pressure monitor, *J. Hum. Hypertens.* 27 (3) (2013) 204–210.
- [17] B.E. Westerhof, et al., Individualization of transfer function in estimation of central aortic pressure from the peripheral pulse is not required in patients at rest, *J. Appl. Physiol.* 105 (6) (Oct. 2008) 1858–1863.
- [18] Y. Zhang, H. Asada, Blind system identification of no coprime multichannel systems and its application to noninvasive cardiovascular monitoring, *ASME J. Dyn. Syst.: Meas. Control* 126 (4) (Dec. 2004) 834–847.
- [19] Q. Mayyala, et al., Structure-based subspace method for multi-channel blind system identification, *IEEE Signal Process. Lett.* 24 (8) (Feb. 2017) 1183–1187.
- [20] A. Patel, et al., Aortic pressure estimation using blind identification approach on single input multiple output nonlinear wiener systems, *IEEE Trans. Biomed. Eng.* 65 (6) (Jun. 2018) 1193–1200.
- [21] T. Mei, Blind multichannel identification based on Kalman filter and eigenvalue decomposition, *Int. J. Speech Technol.* 22 (1) (Mar. 2019) 1–11.
- [22] L. Xu, et al., Baseline wander correction in pulse waveforms using wavelet-based cascaded adaptive filter, *Comput. Biol. Med.* 37 (5) (May. 2007) 716–731.
- [23] W. Huh, et al., Development of pulse rate detection system for oriental medicine, in: *Proceedings of 19th International Conference-IEEE/EMBS*, October 1997, pp. 2406–2408.
- [24] Y. Yao, et al., Validation of an adaptive transfer function method to estimate the aortic pressure waveform, *IEEE J. Biomed. Health Inform.* 21 (2017) 61599–1606.
- [25] R. Burattini, K.B. Campbell, Modified asymmetric T-tube model to infer arterial wave reflection at the aortic root, *IEEE Trans. Biomed. Eng.* 36 (8) (Aug. 1989) 805–814.
- [26] M.K. Abed, et al., Blind system identification, *Proc. IEEE* 85 (12) (Sep. 1997) 1310–1332.
- [27] M.I. Gurelli, C.L. Nikias, A new eigenvector-based algorithm for multichannel blind deconvolution of input coloured signal, in: *IEEE International Conference on Acoustics*, 1993, pp. 448–451. April.
- [28] M. Lustig, et al., Compressed sensing MRI, *IEEE Signal Process. Mag.* 25 (2) (2008) 72–82.
- [29] F.J. Herrmann, G. Hennenfent, Non-parametric seismic data recovery with curvelet frames, *Geophys. J. Int.* 173 (1) (2008) 233–248.
- [30] Y. Sato, A method of self-recovering equalization for multilevel amplitude-modulation systems, *IEEE Trans. Commun.* 23 (6) (2008) 679–682.
- [31] D. Godard, Self-recovering equalization and carrier tracking in two-dimensional data communication systems, *IEEE Trans. Commun.* 28 (11) (1980) 1867–1875.
- [32] J.J. Shynk, et al., Comparative performance study of several blind equalization algorithms, *Proc. SPIE* 1565 (1991) 102–117.
- [33] S.G. Shroff, et al., Physiological relevance of T-tube model parameters with emphasis on arterial compliances, *Am. J. Physiol. Heart Circ. Physiol.* 269 (2) (Aug. 1995) 365–374.
- [34] K.B. Campbell, et al., Time-domain formulation of asymmetric T-tube model of arterial system, *Am. J. Physiol. Heart Circ. Physiol.* 258 (6 Pt 2) (1990) 1761–1774.
- [35] P. Segers, et al., Individualizing the aorto-radial pressure transfer function: feasibility of a model-based approach, *Am. J. Physiol. Heart Circ. Physiol.* 279 (2) (2000) 542–549.
- [36] D.R. Morgan, et al., On the evaluation of estimated impulse responses, *IEEE Signal Process. Lett.* 5 (7) (1998) 174–176.
- [37] M.K. Hasan, et al., Improving robustness of blind adaptive multichannel identification algorithms using constraints, in: *European Signal Processing Conference, IEEE*, 2005, pp. 4–8. September.
- [38] Y.T. Shih, et al., Application of the N-point moving average method for brachial pressure waveform-derived estimation of central aortic systolic pressure, *Hypertension* 63 (4) (Apr. 2014) 865–870.
- [39] E. O'Brien, et al., Working group on blood pressure monitoring of the European society of hypertension international protocol for validation of blood pressure measuring devices in adults, *Blood Press Monit.* 7 (1) (2002) 3–17.
- [40] W. Liu et al., Aortic pressure waveforms reconstruction using simplified Kalman filter, in *Computing in Cardiology*, 2019, no. September, pp. 1–4.
- [41] K.A. Phillips, et al., Why primate models matter, *Am. J. Primatol.* 76 (9) (2014) 801–827.
- [42] M.J. Zurbano, et al., Differences and similarities in tyrosine phosphorylation of proteins in platelets from human and pig species, *J. Thromb. Haemost.* 1 (11) (2010) 2411–2418.
- [43] H. Eisler, Psychophysical similarities between rats and humans, *Bull. Psychon. Soc.* 16 (2) (1980) 125–127.
- [44] M. De Melis, et al., Blood pressure waveform analysis by means of wavelet transform, *Med. Biol. Eng. Comput.* 47 (2) (2009) 165–173.
- [45] R. Kelly, et al., Non-invasive registration of the arterial pressure pulse waveform using high-fidelity applanation tonometry, *J. Vasc. Med. Biol.* 1 (1989) 142–149.
- [46] R. Kelly, et al., Non-invasive determination of age-related changes in human arterial pulse, *Circulation* 80 (1989) 1652–1659.
- [47] R. Kelly, et al., Nitroglycerine has more favorable effects on left ventricular afterload than apparent from measurement of pressure in a peripheral artery, *Eur. Heart J.* 11 (1990) 328–333.
- [48] M.E. Safar, P. Laurent, Pulse pressure and arterial stiffness in rats: comparison with humans, *Am. J. Physiol. Heart Circ. Physiol.* 285 (4) (2003) H1363–H1369.